2016 IEEE International Conference on Robotics and Automation (ICRA)
Stockholm, Sweden, May 16-21, 2016

Generation and Real-Time Implementation of High-Speed Controlled Maneuvers Using an Autonomous 19-Gram Quadrotor

Ying Chen and Néstor O. Pérez-Arancibia

***Abstract*— We present a new experimental method for the generation and real-time implementation of high-speed aerobatic maneuvers, including multiple flips, on a 19-gram autonomous quadrotor. A key element in the proposed approach is the design and experimental tuning of a gain scheduling control strategy in which two *linear time-invariant* (LTI) controllers are alternatingly activated and deactivated to switch between a normal flight mode and an aerobatic mode, enabling the flyer to perform consecutive multiple flips in a robustly stable manner. The implementation of the controllers is done using on-board power, sensors and computing capabilities, so that the quadrotor remains fully autonomous during flight. Notably, the attainment of autonomy, using real-time control, is made possible by the development of a new method for speed planning based on cubic functions, the geometric generalization of the notion of multi-flip and the empirical identification of the flyer's dynamics, required for trajectory generation and controller synthesis. Compelling experimental results demonstrate the suitability of the proposed approach. In particular, we present maneuvers that include consecutive single, double, and triple flips about the flyer's roll principal axis and a non-principal axis. To the best of our knowledge, to this date, the flyer used in this research is the smallest controlled quadrotor to have autonomously accomplished three consecutive flips while remaining stable.**

I. Introduction

A significant amount of research on *micro unmanned aerial vehicles* (MUAVs) has been published during the last few years. In particular, multi-rotors have been used to create a wide variety of research platforms, with notable success in highly structured flying arenas instrumented with motion-capture systems such as Vicon [1]. Relevant improvements in the design and fabrication of powerful microprocessors, MEMS sensors, ultralight electric motors and micro Li-Po batteries have made possible the development of small-sized rotor-based aircraft, such as helicopters and quadrotors, motivating innovative research in a gamut of technological areas. For example, a study on the aerodynamics of a quadrotor flown by the automatic action of a *proportional-integral-derivative* (PID) controller is presented in [2], the application of adaptive control to the flight of quadrotors subjected to failure produced by the loss of thrust is discussed in [3], machine learning algorithms for the generation and control of high-speed maneuvers on a helicopter are described in [4], the use of iterative learning control for the implementation of aerobatic maneuvers on quadrotors is presented in [5] and [6]. Similarly, quadrotors and their dynamics have been employed extensively to test flight control methods for the real-time implementation of single-flip maneuvers [7], [8], [9], [10].

The main objective of the research discussed in this paper is the development of new experimental methods for the generation and real-time implementation of high-speed maneuvers, required for the creation of high-level control primitives [11] that will enable the creation of fully autonomous robotic flyers capable of operating and *surviving* in highly unstructured environments. Specifically, we propose a gain-scheduling-based control strategy [12] for the implementation of high-speed multi-flip aerobatic maneuvers on a 19-gram quadrotor (including its battery) with a *propeller-tip-to-propeller-tip* (PTPT) distance of 13 cm and a thrust-to-weight ratio of 1.7. Multi-flip maneuvers require rapid acceleration and deceleration of the flyer's angular velocity, and rapid robust stabilization to avoid vehicle stall, while operating in the presence of aerodynamic disturbances and motor latency. We show that the control of multi-flip maneuvers is essentially a rapid version of the attitude control of a rigid body. Based on this notion, we introduce a specialized angular-speed planning method that, combined with the proposed gain-scheduling control strategy, make possible the robustly stable control of the experimental quadrotor, while maneuvering at high speeds. Notice that not only is this flyer smaller and lighter, it also has a lower thrust-to-weight ratio, a larger motor time constant, and significantly less computing power than typical quadrotors used in high-speed aerobatic research, as for example those in [5] and [6]. Furthermore, in this research we are only using the quadrotor's own on-board sensing capabilities as opposed to using motion-capture systems such as Vicon [5], [6], [13], [14], [15] in highly-structured arenas or employing heavily-instrumented flyers in outdoor arenas [16], [17]. All that mentioned above makes the process of synthesizing controllers for the case considered here very experimentally challenging.

In general, compared to normal-sized quadrotors (with PTPT distances of 35 cm to 70 cm, weighing 0.25 Kg to 2 Kg), a small quadrotor can be more easily affected by external aerodynamic disturbances because of its relatively smaller mass and moment of inertia. Additionally, in the case considered here, limited by the flyer's overall small size and low thrust-to-weight ratio, essential components of the quadrotor, such as motors, sensors and power source, are stringently constrained in size, weight and performance. In [15], a quadrotor with a similar size was demonstrated to accomplish double flips. However, those results were obtained with the implementation of more powerful motors, a multi-camera motion-capture system (Vicon), employed as an external sensor to measure position and velocity, and an external station for high-level planning and control. In contrast, in the research presented in this paper, all the sensors used in control loops are carried by the flyer and all the algorithms for signal processing and control are run on-board. To the best of our knowledge, the flyer used in this research is the smallest controlled quadrotor to have accomplished three consecutive triple flips, flying autonomously from the power and control perspectives, while remaining stable.

The maximum flipping speed employed in this research is $2.5 \cdot 10^3$ deg $\cdot$ s^{-1} and the proposed control method is empirically tested and demonstrated robust, from the stability

This work was supported by the USC Viterbi School of Engineering through a graduate fellowship to Y. Chen and a start-up fund to N. O. Pérez-Arancibia.

The authors are with the Department of Aerospace and Mechanical Engineering, University of Southern California (USC), Los Angeles, CA 90089-1453, USA (e-mail: chen061@usc.edu; perezara@usc.edu).

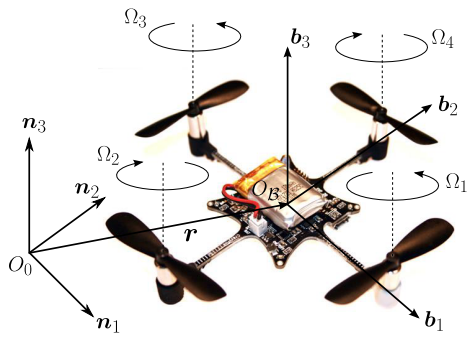

Fig. 1: Frames of reference. $\mathcal{N} = \{\boldsymbol{O}_0, \boldsymbol{n}_1, \boldsymbol{n}_2, \boldsymbol{n}_3\}$ is the inertial frame, $\mathcal{B} = \{\boldsymbol{O}_{\mathcal{B}}, \boldsymbol{b}_1, \boldsymbol{b}_2, \boldsymbol{b}_3\}$ is the body frame, $\boldsymbol{r}$ indicates the position of the flyer's center of mass from the inertial origin $\boldsymbol{O}_0$ and $\{\Omega_1, \Omega_2, \Omega_3, \Omega_4\}$ are the angular speeds of the rotors.

and performance standpoint, for a single flip, double flips, and triple flips. We believe that this is a significant step toward the goal of creating entirely autonomous flying *nano* quadrotors (weighing less than 30 g) because the controller proposed here can operate using on-board sensors, actuators and computational capabilities only. This technological achievement is made possible by the development of new methods for angular speed planning and controller synthesis, and the geometric generalization of multi-flipping angle and multi-flip maneuver. Such generalization enables the flyer to perform multi-flips about its principal axes as well as any non-principal axis passing through the flyer's center of mass, provided that the right controller structure and gains are programmed into the on-board micro controller. As an example, here, we present maneuvers that include a single flip, double flips and triple flips about the axis that deviates 45° from the principal axis $\boldsymbol{b}_1$ on the $\boldsymbol{b}_1$-$\boldsymbol{b}_2$-plane.

The rest of paper is organized as follows. Section II models the dynamics of the flying system and explains the composing phases of a multi-flip maneuver, Section III describes the micro unmanned aerial vehicle and experimental setup, the control strategy is introduced in Section IV, experimental results are presented and discussed in Section V. Lastly, some conclusions are drawn in Section VI.

II. Model of the System Dynamics

In this section, we discuss the two dynamical models used to synthesize controllers for the quadrotor, which operates in two distinctive modes, multi-flip aerobatic flight and regular flight. The first model is a complex nonlinear dynamical description of the flyer. The second model assumes small attitude angles and slow angular velocities to linearize the nonlinear dynamics of the first model. Both models are used in the implementation of multi-flip aerobatic trajectories, defined as flying processes which start at a stable hover, transition to a multi-flip aerobatic maneuver, and return to a stable hover.

A. Quadrotor Dynamics

The quadrotor employed in this research is shown in Fig. 1. To determine the dynamics of this MUAV, we define the inertial frame $\mathcal{N} = \{\boldsymbol{O}_0, \boldsymbol{n}_1, \boldsymbol{n}_2, \boldsymbol{n}_3\}$ and the body-fixed frame $\mathcal{B} = \{\boldsymbol{O}_{\mathcal{B}}, \boldsymbol{b}_1, \boldsymbol{b}_2, \boldsymbol{b}_3\}$, which has its origin and axes coinciding with the center of mass and principal axes of the MUAV, respectively. The frames $\mathcal{N}$ and $\mathcal{B}$ are related to each other through the Euler angles $\{\psi, \theta, \phi\}$ in the Z-Y-X convention with the origin of $\mathcal{B}$, $\boldsymbol{O}_{\mathcal{B}}$, at position $\boldsymbol{r}$ from the inertial origin $\boldsymbol{O}_0$. Thrust is generated by four rotating propellers with angular speeds $\{\Omega_1, \Omega_2, \Omega_3, \Omega_4\}$. Using this convention, it follows that the nonlinear dynamics of the flyer are given by

$$m\ddot{\boldsymbol{r}} = -mg\boldsymbol{n}_3 + f\boldsymbol{b}_3, \tag{1}$$
$$J\dot{\boldsymbol{\omega}} = -\boldsymbol{\omega} \times J\boldsymbol{\omega} + \boldsymbol{\tau}, \tag{2}$$
$$\dot{S} = S\hat{\boldsymbol{\omega}}, \tag{3}$$

where m is the total mass of the flyer, J is the diagonal matrix of inertia of the robot with respect to the axes of $\mathcal{B}$, g is the acceleration of gravity constant, $f = \sum_{i=1}^{4} f_i$ is the magnitude of the total thrust force produced by the four propellers, $\boldsymbol{\omega}$ is the quadrotor's angular velocity with respect to $\mathcal{N}$ with its components expressed in $\mathcal{B}$, $\boldsymbol{\tau}$ is the total torque applied by the rotors to the vehicle and S is the active rotation matrix associated with the flyer's movement in space, as defined in Page 32 of [18]. In (3), the *hat* operator maps the vector $\boldsymbol{\omega} = \begin{bmatrix} \omega_1 & \omega_2 & \omega_3 \end{bmatrix}^T$ to a skew-symmetric matrix, as defined in Page 411 of [18].

In the model described by (1)-(3), we ignore the aerodynamic effects produced by the flyer's translational motion and combined gyroscopic effects caused by the rotations of the rotors and the vehicle's body. The direction of the thrust force is assumed to be perpendicular to the $\boldsymbol{b}_1$-$\boldsymbol{b}_2$ plane, along the $\boldsymbol{b}_3$ axis, by ignoring the blade-flapping effect. The nonlinear dynamical model in (1)-(3) is mainly employed in the development of the controller used during the performance of multi-flip aerobatic maneuvers.

The second dynamical model discussed in this section is a linearized version of the nonlinear dynamics in (1)-(3), valid for small body-attitude angles and slow body angular velocities, which are reasonable assumptions of regular flight mode. Since the body angular velocities are assumed to be slow and Euler angles small, it follows that (1)-(3) can be approximated by computing the derivatives of the Euler angles with respect to time, yielding

$$m\ddot{x} = f\cos\psi\sin\theta, \tag{4}$$
$$m\ddot{y} = -f\cos\psi\sin\phi, \tag{5}$$
$$m\ddot{z} = f - mg, \tag{6}$$
$$J_{11}\ddot{\phi} = \tau_1, \tag{7}$$
$$J_{22}\ddot{\theta} = \tau_2, \tag{8}$$
$$J_{33}\ddot{\psi} = \tau_3, \tag{9}$$

where $\{J_{11}, J_{22}, J_{33}\}$ are the diagonal entries of the inertia diagonal matrix J, $\{\tau_1, \tau_2, \tau_3\}$ are the components of $\boldsymbol{\tau}$ expressed in $\mathcal{B}$ and $\{x, y, z\}$ are the components of $\boldsymbol{r}$ with respect to $\mathcal{N}$. Notice that this model is considered linear because (7)-(9) can be solved independently of (4)-(6) and independently of each other, and therefore, ϕ, θ and ψ can be considered inputs to (4)-(6). As mentioned above, this linearized model is used to design the controller employed by the quadrotor when it operates at the regular flight mode. To construct the control inputs, the magnitudes of the thrust force and reaction moment generated by the ith rotor are approximated as

$$f_i = k_f\Omega_i^2, \tag{10}$$
$$\mu_i = k_\mu\Omega_i^2, \tag{11}$$

with $i = 1, \cdots, 4$, where k_f and k_μ are experimentally determined coefficients of thrust-force and reaction-torque, respectively. Thus, from physical first principles and simple

TABLE I: Experimentally Measured and Identified Parameters of the Flyer's Dynamical Models.

m	$19\,\mathrm{g}$
J_{11}	$1.0968 \times 10^{-5}\,\mathrm{kg \cdot m^2}$
J_{22}	$1.0195 \times 10^{-5}\,\mathrm{kg \cdot m^2}$
J_{33}	$1.3905 \times 10^{-5}\,\mathrm{kg \cdot m^2}$
d	$42.68\,\mathrm{mm}$
k_μ	$7.1834 \times 10^{-11}\,\mathrm{kg \cdot m^2 \cdot rad^{-2}}$
k_f	$1.7518 \times 10^{-8}\,\mathrm{kg \cdot m \cdot rad^{-2}}$

algebraic manipulations, we obtain that

$$\begin{bmatrix} f \\ \tau_1 \\ \tau_2 \\ \tau_3 \end{bmatrix} = \begin{bmatrix} k_f & k_f & k_f & k_f \\ 0 & -k_f d & 0 & k_f d \\ -k_f d & 0 & k_f d & 0 \\ -k_\mu & k_\mu & -k_\mu & k_\mu \end{bmatrix} \begin{bmatrix} \Omega_1^2 \\ \Omega_2^2 \\ \Omega_3^2 \\ \Omega_4^2 \end{bmatrix}, \quad (12)$$

where d is the shortest distance from a rotor center of rotation to the robot's center of mass. All the parameters required to complete the nonlinear model in (1)-(3) and the linearized model in (4)-(9) were experimentally measured or identified through static and dynamic experiments. The list of estimated parameters is summarized in Table I.

From (10)-(12), it clearly follows that the rotor speeds Ω_i, for $i = 1, \cdots, 4$, determine the inputs to both the nonlinear model given by (1)-(3) and linearized system described by (4)-(9). Consequently, it is crucial to understand the dynamics associated with the rotor speeds Ω_i. In a first approximation, we assume that the angular speed, Ω, of a generic rotor of the kind considered here can be modeled as the output from a first-order system with the form

$$\dot{\Omega} = k_\Omega \left(\Omega_\mathrm{d} - \Omega\right), \quad (13)$$

where the rotor speed $\Omega(t)$ is the output, the target speed $\Omega_\mathrm{d}(t)$ is the input and k_Ω is a parameter of the system. In principle, the parameter k_Ω should be empirically identifiable through simple experiments. We perform experiments in which the robot remains stationary while the rotors are excited with a set of Heaviside step functions with different amplitudes. The results from this experiment are shown in Fig. 2, indicating that the value of the parameter k_Ω increases as the amplitude of the target speed $\Omega_\mathrm{d}(t)$ is increased. Thus, we can conclude that the structure in (13) cannot capture the true dynamics of the rotor. Also, in the step responses of Fig. 2, it can be seen that the settling time is in the range $[0.4, 1.0]$ s, which is a stringent constraint on the high-speed capabilities of the flyer. This point becomes clear by noticing that, as shown latter in Section V, a multi-flip aerobatic maneuver can take as much as 1.0 s. Thus, the relatively slow actuator response represents a major limitation in the real-time implementation of high-speed maneuvers.

B. The Process of a Multi-Flip Maneuver

As shown in Fig. 3, a multi-flip maneuver is a process that can be divided into three phases, climb, multi-flip, and descent and re-stabilization. When the robot is rotating in the air it starts to fall because the thrust forces generated by the rotors are not aligned vertically and the flyer's weight is not compensated. The climb phase is necessary because it can provide extra distance to avoid collisions with ground and an upward speed to reduce the falling distance. The multi-flip phase starts when the control references for the robot's angular velocity and acceleration are varied so that it is forced to rotate about a chosen body axis. The multi-flip phase ends when the flipping angle reaches an *a priori*

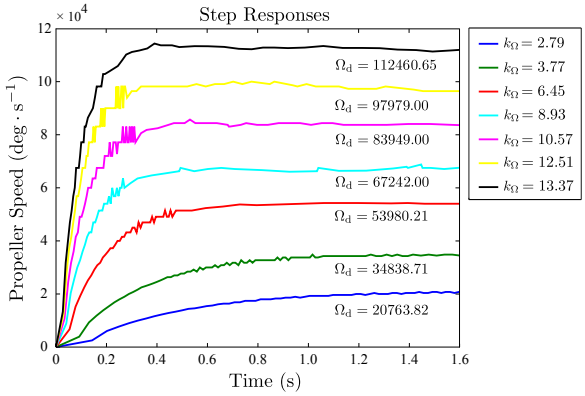

Fig. 2: Step response of the rotor speed for seven different step inputs. The rotor speed is measured using a high-speed camera at $3,000$ fps. The variable k_Ω is the parameter of the first-order model of the rotor dynamics in (13).

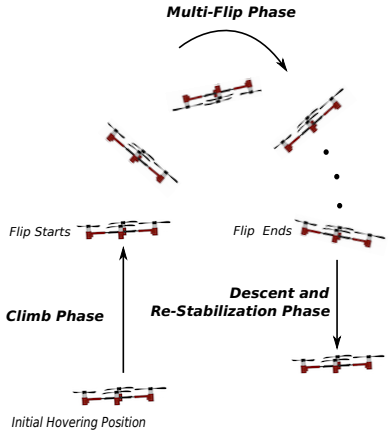

Fig. 3: The whole process of a multi-flip maneuver is composed of three phases, the climb phase, multi-flip phase, and descent and re-stabilization phase. At the beginning, the quadrotor is hovering at a certain altitude and then is triggered to start the multi-flip maneuver. All three phases are autonomously controlled through only on-board sensors and controller.

defined target angle, typically $2n\pi$, where n is referred to as the number of flips. In most cases, the angular velocity of the quadrotor is not zero at the end of the multi-flip phase, and for this reason, the descent and re-stabilization phase is primarily used to re-stabilize the robot's attitude and stop its rapid fall. Clearly, height and time impose very stringent constraints on the flyer capabilities, which is especially true for the robot employed here (the Crazyflie shown in Fig. 1) because it has a very low thrust-to-weight ratio of 1.7.

III. Experimental Setup

A. The Flying Vehicle

For the experiments discussed in this paper we use a Crazyflie 1.0 nano-quadrotor manufactured by Bitcraze AB [19] (shown in Fig. 1), which has a PTPT distance of 13 cm, weighs 19 g (including the battery) and a flight endurance of approximately 7 min, achieved with a 170 mAh Li-Po battery. This robot carries several on-board sensors used in the implementation of controllers, including a 3-axis accelerometer, a 3-axis gyroscope and a MEMS barometer. The MEMS barometer measures the altitude of the robot while the accelerometer and gyroscope are used to estimate the robot's attitude and generate the angular velocity signal used as feedback. The measurement range of the gyroscope is $\pm 2 \cdot 10^3$ deg $\cdot$ s^{-1}, an important parameter considered in the discussion about controller design in Section IV.

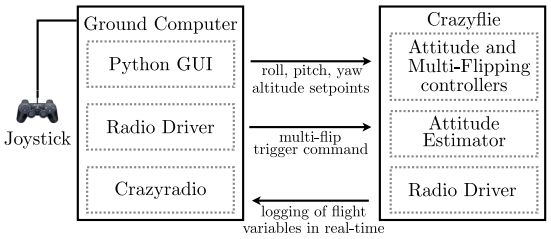

Fig. 4: Architecture of the experimental setup. The ground computer and joystick are mainly used to send references of attitude and altitude to the quadrotor and compensate drift during regular flight. The ground computer is also receives the real-time quadrotor data for off-line analysis.

The flyer also carries on-board computational and communications capabilities, essential for the implementation of real-time controllers. The communications chip has a nominal transmission bandwidth of 2 Mbit$\cdot$s^{-1} and the *micro controller unit* (MCU) runs at 72 MHz, employing 128 KB of flash memory and 20 KB of RAM. The flying system is actuated with micro coreless DC electrical motors, generating a *thrust-to-weight ratio* (TWR) of approximately 1.7. The TWR is relatively small and consistent with the large settling times shown in Fig. 2, discussed in Section II-A. Notice that the limited actuation capabilities available make the proposed control problem challenging and interesting, as it takes a relatively long time for the robot to generate the thrust forces required to stabilize itself after completing a multi-flip aerobatic maneuver.

B. Experimental Control and Communications Architecture

The basic control and communications architecture of the experimental setup, consisting of a joystick, a ground computer and the quadrotor, is shown Fig. 4. The ground computer and joystick are used to send reference signals for the altitude and body-attitude angles (roll-angle, pitch-angle and yaw-angle) of the quadrotor during regular flight mode. Simultaneously, algorithms that control the robot's altitude and attitude run using the information sensed by the on-board barometer, accelerometer and gyroscope. The sensor data from the accelerometer and gyroscope are filtered using an attitude estimator [20] before being sent as input to the controller. The raw data from the gyroscope is also sent to the controller as an input for error calculation. Employing the scheme in Fig. 4, the measured flight variables, such as the Euler angles and flipping angular velocity can be communicated from the flyer to the ground computer in real time for monitoring purposes. During regular autonomous hovering, the quadrotor uses the altitude information from the barometer and the estimated attitude for feedback in the on-board control loops. Using the joystick, the motions on the $\boldsymbol{n}_1$-$\boldsymbol{n}_2$ plane, i.e, (x, y), are manually controlled from the ground by varying the roll-angle and pitch-angle references. From this flight mode a multi-flip aerobatic maneuver is triggered by a command sent from the ground computer. During the aerobatic maneuver, the robot operates completely autonomously, relying entirely on on-board sensing, signal processing and control, and no reference commands are sent from the ground to the flyer until the three phases of the multi-flip maneuver are completed. The control strategy and the controller synthesis method are discussed in Section IV below.

IV. Multi-Flip Planning and Controller Design

A. Generalized Multi-Flip and Generalized Flipping Angle

Normally, the notion of multi-flip maneuver refers to a $2n\pi$ angle rotation about the $\boldsymbol{b}_1$ (roll) or $\boldsymbol{b}_2$ (pitch) principal axis of the flyer, where the integer n indicates the number of consecutive flips [5], [6], [15]. Here, we generalize the concept of multi-flip maneuver to any body-fixed axis passing through the flyer's center of mass. A *generalized flipping angle* is defined as the angle with its vertex in the flipping axis, measured in the plane perpendicular to the flipping axis, generated between the horizontal plane of the inertial frame ($\boldsymbol{n}_1$-$\boldsymbol{n}_2$-plane) and the line created by the intersection of the $\boldsymbol{b}_1$-$\boldsymbol{b}_2$-plane with the plane perpendicular to the flipping axis (intersection line for short). The direction of the flipping axis with respect to the inertial frame determines the sign of the generalized flipping angle following the right-hand principle. This definition is very similar to the definition of the roll-angle in the Euler Z-Y-X convention. In fact, the generalized flipping angle is equal to the *new* Euler roll-angle after rotating the axis $\boldsymbol{b}_1$ to match the flipping axis and the axis $\boldsymbol{b}_2$ to match the line created by the intersection of the $\boldsymbol{b}_1$-$\boldsymbol{b}_2$-plane with the plane perpendicular to the flipping axis. The multi-flip axis is described by the unit vector $\boldsymbol{a}_\mathrm{f} = \begin{bmatrix} a_1 & a_2 & a_3 \end{bmatrix}^T$, fixed to the robot's body and written with respect to $\mathcal{B}$, so that $a_1^2 + a_2^2 + a_3^2 = 1$. The *new* attitude quaternion [21], obtained after the axes $\boldsymbol{b}_1$ and $\boldsymbol{b}_2$ are re-aligned along the generalized flipping axis and intersection line, respectively, can be computed as

$$q' = q * u = \begin{bmatrix} q'_0 & q'_1 & q'_2 & q'_3 \end{bmatrix}, \tag{14}$$

where $*$ denotes the quaternion product [21], the quaternion q expresses the current attitude of the robot and the quaternion u expresses the rotation of $\boldsymbol{b}_1$ and $\boldsymbol{b}_2$ required to coincide with the generalized flipping axis and the intersection line, respectively. Notice that the components of u directly depend on the components of $\boldsymbol{a}_\mathrm{f}$, but for the sake of brevity here we omit the explicit expression that relates them to each other. Using quaternion notation, the generalized flipping angle is given by

$$\phi_\mathrm{g} = \arctan \frac{2(q'_0 q'_1 + q'_2 q'_3)}{q'^2_0 - q'^2_1 - q'^2_2 + q'^2_3}. \tag{15}$$

Notice that this quaternion expression of ϕ_g is very convenient for programming the on-board control algorithms.

It is important to note that since the MEMS gyroscope possesses limited sensing capabilities ($\pm 2 \cdot 10^3$ deg $\cdot$ s^{-1}) and is mounted right on top of the principal axes, when the generalized flipping axis is not aligned with a principal axis, the generalized flipping speed can exceed the sensor limits. For instance, if the generalized flipping axis is chosen to be $\boldsymbol{a}_\mathrm{f} = \begin{bmatrix} 1/\sqrt{2} & 1/\sqrt{2} & 0 \end{bmatrix}^T$, the maximum generalized flipping speed is $2\sqrt{2} \cdot 10^3$ deg $\cdot$ s^{-1}. This is a stringent limitation, since the maximum number of flips that the robot can achieve in a given amount of time directly depends on the maximum achievable flipping speed.

B. Flipping Speed Planning

The implementation of multi-flip maneuvers is an interesting way to test the quadrotor flight capabilities and the suitability of the proposed real-time control schemes. Flipping demonstrates the practical controllability of the robot's attitude, since a complex rigid-body attitude reference has to be followed in an extremely short time while avoiding collisions and preventing stall. To prevent stall, it is better to control the flipping angular speed rather than the flipping angle [6]. Since a single-flip maneuver takes up to 0.5 s, and a triple-flip maneuver takes up to 1.0 s, it is necessary to take into account the rotors' dynamical behavior and carefully plan the flipping speed to make it compatible with the actuators' performances. Notice that the reference flipping

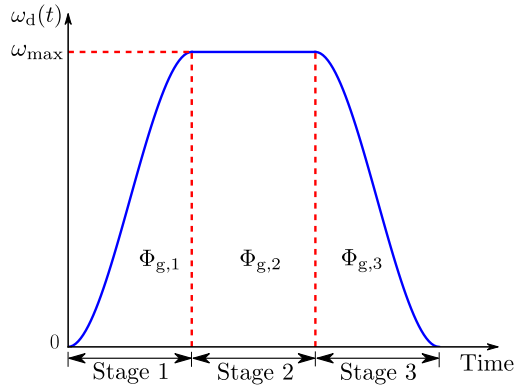

Fig. 5: Generalized flipping speed reference, $\omega_{\mathrm{d}}(t)$. This signal is composed of three sections, corresponding to the three stages of the multi-flip phase in Fig. 3. The symbols $\Phi_{\mathrm{g},1}$, $\Phi_{\mathrm{g},2}$ and $\Phi_{\mathrm{g},3}$ denote the amount of rotation accumulated during each of the three stages, corresponding to the area under the function $\omega_{\mathrm{d}}(t)$ aggregated during each stage. The total area under the function $\omega_{\mathrm{d}}(t)$ is $\sum_{i=1}^{3}\Phi_{\mathrm{g},i} = 2n\pi$, where n is the number of flips. The maximum allowed flipping speed is denoted by $\omega_{\max}$.

speed combined with the direction of the flipping axis define a reference velocity. The reference speed trajectory used in the experiments discussed here is generated to satisfy the actuators' specifications and sensors' limitations, and for this reason, it is smooth and its maximum value is constrained by the constant $\omega_{\max}$. The resulting flipping speed reference signal is composed of three parts, a rising-speed section, a constant-speed section and a decreasing-speed section, as shown in Fig. 5. The reason for including the second section is the limited capability of the MEMS gyroscope to measure angular velocities.

In Fig. 5, the first and third sections of the flipping velocity reference are generated using cubic functions to guarantee that the angular acceleration remains continuous during the entire flip maneuver. In contrast, in other published experimental cases [6], the flipping speed references are composed of linear functions, which induce acceleration discontinuities during the occurrence of flip maneuvers. The gradual increase and decrease of the flipping speed reference in Fig. 5 satisfy the specifications and limitations of the rotors. Consistently, the first section of the flipping speed reference is constructed as

$$\omega_{\mathrm{d},1}(t) = \frac{\beta_1}{3}\left(t-\gamma_1\right)^3 - \beta_1\gamma_1^2 t + \frac{\beta_1\gamma_1^3}{3}, \tag{16}$$

with $\gamma_1 = \omega_{\max}^{-1}\Phi_{\mathrm{g},1}$, $\beta_1 = -3/4\cdot\gamma_1^{-3}\omega_{\max}$ and $\dot{\omega}_{\max,1} = 3/4\cdot\Phi_{\mathrm{g},1}^{-1}\omega_{\max}^2$, where $\Phi_{\mathrm{g},1}$ is the desired amount of rotation generated during Stage 1 (first section of $\omega_{\mathrm{d}}(t)$) and $\dot{\omega}_{\max,1}$ is the maximum flipping angular acceleration in the first section of ω_{d}, which must remain smaller than the maximum angular acceleration about the generalized flipping axis that the sensing system can measure. The time-duration of the first section of ω_{d}, $\omega_{\mathrm{d},1}$, is $\delta_1 = 2\gamma_1$, which is completed when both $\Phi_{\mathrm{g},1}$ and $\omega_{\max}$ are reached. To continue with the construction of ω_{d}, we define the second section as

$$\omega_{\mathrm{d},2}(t) = \omega_{\max}, \tag{17}$$

with the associated time-duration $\delta_2 = \omega_{\max}^{-1}\Phi_{\mathrm{g},2}$, where $\Phi_{\mathrm{g},2}$ is the desired amount of rotation generated during Stage 2 (second section of $\omega_{\mathrm{d}}(t)$), as illustrated in Fig. 5. To complete the construction of $\omega_{\mathrm{d}}(t)$, we define the third section as

$$\omega_{\mathrm{d},3}(t) = \frac{\beta_3}{3}\left(\gamma_3+\delta_2'-t\right)^3 - \beta_3\gamma_3^2\left(2\gamma_3+\delta_2'-t\right) + \frac{\beta_3\gamma_3^3}{3}, \tag{18}$$

with $\gamma_3 = \omega_{\max}^{-1}\Phi_{\mathrm{g},3}$, $\beta_3 = -3/4\gamma_3^{-3}\omega_{\max}$ and $\dot{\omega}_{\max,3} = 3/4\Phi_{\mathrm{g},3}^{-1}\omega_{\max}^2$, where $\Phi_{\mathrm{g},3}$ is the desired amount of rotation generated during Stage 3 (third section of $\omega_{\mathrm{d}}(t)$) and $\dot{\omega}_{\max,3}$ is the maximum flipping angular acceleration in the third section of $\omega_{\mathrm{d}}(t)$, which must remain smaller than the maximum angular acceleration about the generalized flipping axis that the sensor can measure, and δ_2' is the actual end time of Stage 2 in Fig. 5. Similarly to the case in Stage 1, the time-duration of Stage 3 is $\delta_3 = 2\gamma_3$, completed when $\Phi_{\mathrm{g},3}$ is reached.

The trajectory planning method introduced in this section, illustrated in Fig. 5, corresponds to the multi-flip phase discussed in Section II-B. Thus, once the multi-flip maneuver is completed, the control reference for the generalized flipping speed is set back to zero. In the construction of $\omega_{\mathrm{d}}(t)$, the parameters needed to be specified *a priori* are $\Phi_{\mathrm{g},1}$, $\Phi_{\mathrm{g},2}$, $\Phi_{\mathrm{g},3}$ and $\omega_{\max}$. There are two things to consider when specifying the above four parameters. The first one is that the angular accelerations during the first and third stages must not exceed the nominal maximum angular acceleration, and normally, $\dot{\omega}_{\max,3}$ should be smaller than $\dot{\omega}_{\max,1}$. The second consideration is that the nominal amount of time needed to complete a multi-flip maneuver should be minimized while satisfying the constraints already discussed above.

C. Altitude Change Analysis

Having discussed the trajectory planning for the generalized flipping speed, now we analyze and estimate the required climbing and descending distances to successfully complete a multi-flip maneuver. We assume that the actual time-duration of a multi-flip maneuver is equal to the nominal value and that the vertical acceleration during flipping is equal to the gravitational acceleration. The amount of time spent in each of the three phases in Fig. 3 are denoted by Δt_1, Δt_2 and Δt_3, respectively. In this scheme, Δt_1 is specified *a priori* and determines the climbing distance, which can be estimated as

$$d_{\text{climb}} = \frac{1}{2}g\left(\Delta t_1\right)^2\left(\eta^2-\eta\right), \tag{19}$$

where η is the nominal maximum thrust-to-weight ratio. The time duration of the second phase depends on the shape of $\omega_{\mathrm{d}}(t)$ and is given by

$$\Delta t_2 = \frac{2\Phi_{\mathrm{g},1}+\Phi_{\mathrm{g},2}+2\Phi_{\mathrm{g},3}}{\omega_{\max}} = \frac{4n\pi-\Phi_{\mathrm{g},2}}{\omega_{\max}}, \tag{20}$$

where n indicates the number of flips to be performed by the quadrotor. Assuming that the quadrotor reaches the peak altitude before the second phase ends, it follows that

$$\Delta t_3 = \frac{\Delta t_2-(\eta-1)\Delta t_1}{\eta-1}, \tag{21}$$

which determines the descent time, estimated as

$$d_{\text{descent}} = \frac{1}{2}g\left(\Delta t_3\right)^2\left(\eta^2-\eta\right). \tag{22}$$

Notice that (19)-(22) indicate that for large values of $\omega_{\max}$ and η, the total amount of time required to perform a multi-flip maneuver is small, and conversely, for small values of $\omega_{\max}$ and η, the total amount of time required to perform a multi-flip maneuver is large. Recalling that $\omega_{\max}$ is constrained by the maximum value that the on-board sensors can measure and that η is constrained by the thrust forces that the rotors can generate, it follows that the aerobatic capabilities of a quadrotor are enabled, and limited, by its sensors and actuators.

D. Controller Design for Multi-Flip Aerobatic Maneuvers

The proposed control scheme is shown in Fig. 6. This scheme is composed of two controllers, one for regular flight, shown in Fig. 6-(a), and other for multi-flip aerobatic flight, shown in Fig. 6-(b). The controller in Fig. 6-(a) is designed using the linearized dynamics of the quadrotor described by (4)-(9) and employs simple SISO[1] PID loops to separately control the Euler angles and the altitude of the robot. In regular flight mode, the translational motion of the quadrotor on the $\boldsymbol{b}_1$-$\boldsymbol{b}_2$-plane can be controlled by varying the pitch- and roll-angles, provided that the yaw-angle is set to zero. The $\boldsymbol{b}_3$ direction translational motion is controlled by varying the thrust force. To map the control inputs to motor commands we employ the inverse of (12) and the linear proportional relationship between PWM[2] signals and rotor speeds. This simple controller is employed during regular flight and during the climb phase shown in Fig. 3.

The controller in Fig. 6-(b) is employed during the multi-flip phase and the descent and re-stabilization phase of the aerobatic maneuver graphically described in Fig. 3. Following a gain-scheduling control strategy, the controller in Fig. 6-(b) turns on as the controller in Fig. 6-(a) turns off when the quadrotor finishes the climb phase in a pre-defined amount time, Δt_1, as shown in Fig. 3. From (19), it directly follows that Δt_1 determines the total climb distance and the vertical speed of the robot when the multi-flip phase starts. Once the multi-flip phase ends, during the third phase of the aerobatic maneuver, the controller in Fig. 6-(b) turns off and the controller in Fig. 6-(a) turns on for the quadrotor to operate back in the regular flight mode. Normally, the more oscillation the angular velocity has after a multi-flip maneuver, the longer it is necessary to wait before switching back to the regular flight mode.

During multi-flip maneuvers, the robot remains completely autonomous from the power and control perspectives, as the control algorithms are run on-board, using information measured with on-board sensors only. In the scheme of Fig. 6-(b), the control error signals used in the feedback loops are defined as

$$\begin{bmatrix} \boldsymbol{e}_\omega(t) \\ \boldsymbol{e}_\alpha(t) \end{bmatrix} = \begin{bmatrix} \boldsymbol{\omega}(t) - \omega_{\mathrm{d}}(t)\boldsymbol{a}_{\mathrm{f}} \\ \{F\boldsymbol{\omega}\}(t) - \dot{\omega}_{\mathrm{d}}(t)\boldsymbol{a}_{\mathrm{f}} \end{bmatrix}, \tag{23}$$

where $\boldsymbol{a}_{\mathrm{f}}$ is the generalized axis unit vector, $\boldsymbol{\omega}$ is the angular velocity measured using the MEMS gyroscope, ω_{d} is the planned generalized multi-flip speed described in Section IV-B, and F is a filter with the form $\lambda s\,(s+\lambda)^{-1}$, with $0 < \lambda \in \mathbb{R}$. The signal $\boldsymbol{e}_\omega$ can be thought of as the angular velocity error and $\boldsymbol{e}_\alpha$ as the angular acceleration error. Then, consistently with Fig. 6-(b), we define

$$\begin{bmatrix} \tau_1 & \tau_2 & \tau_3 \end{bmatrix}^T = -K_\omega \boldsymbol{e}_\omega - K_\alpha \boldsymbol{e}_\alpha, \tag{24}$$

where $\{\tau_1, \tau_2, \tau_3\}$ are the components of $\boldsymbol{\tau}$ in (2), and K_ω, K_α are positive diagonal gain matrices. It is important to note that during a multi-flip maneuver, the total thrust force in (1), f, is set to half of the maximum thrust force in order to avoid motor saturation. Similarly to the case in Fig. 6-(a), after computing $\boldsymbol{\tau}$ and f, the on-board control algorithms compute the inverse of the mapping in (12) to obtain the angular speed of each motor. Since the rotor speed is approximately proportional to the voltage command to the rotors' motors, the command PWM values are easily computable.

In the scheme of Fig. 6-(b), we employ the angular acceleration feedback loop to decrease the oscillation of the angular flipping speed caused by latency in the rotor dynamics. As shown in Fig. 2, the step-response settling time for an individual rotor is between 0.4 s and 1.0 s, which is large compared to the approximately 1.0-s duration of a multi-flip maneuver. It is reasonable to assume that the latency observed in the ground experiments also appears during flight. We believe that the angular acceleration control loop is the key element in the proposed control strategy that enables the quadrotor to perform consecutive triple-flip aerobatic maneuvers autonomously, given that battery power will last.

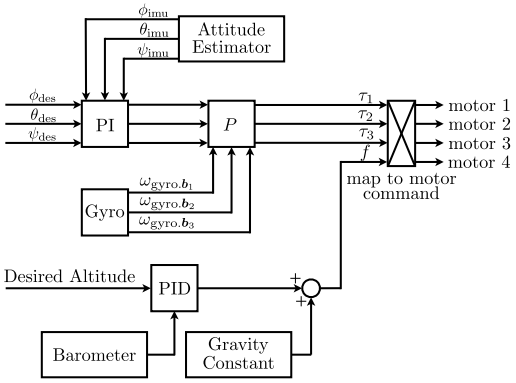

(a) Controller for Regular Flight.

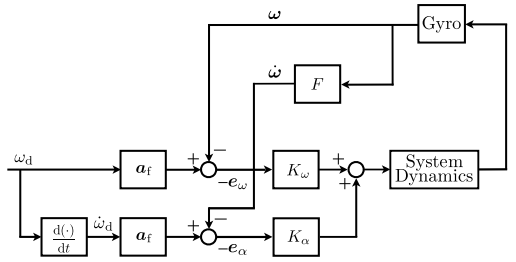

(b) Controller for Multi-Flip Aerobatic Fight.

Fig. 6: Real-time gain-scheduling-based control structure implemented on-board. **(a)** Block diagram of the PID controller used during regular flight and the climb phase. The external inputs are the desired Euler angles $\{\phi_{\mathrm{des}}, \theta_{\mathrm{des}}, \psi_{\mathrm{des}}\}$ and desired altitude. The control signals are computed employing the feedback from the attitude estimator, gyroscope and barometer. The control signals are converted to motor PWM commands through the inverse of the mapping in (12). The matrix operator P combines the outputs from the PI-block and Gyro-block to generate the PID control torque signal $[\tau_1\ \tau_2\ \tau_3]^T$. **(b)** Block diagram of the controller used during the multi-flip and re-stabilization phases, defined in Fig. 3. The flipping speed reference ω_{d} is constructed off-line as described in Section IV-B and illustrated in Fig. 5. The feedback control loops employ both the measured body angular velocity and an estimate of its derivative, computed using real-time data from the MEMS gyroscope. The roles of the operators F, a_{f}, K_ω and K_α are described by (23) and (24).

For practical implementation purposes, during flight, the flipping speed reference, $\omega_{\mathrm{d}}(t)$, is varied using the current measured generalized multi-flip angle, according to the law

$$\omega_{\mathrm{d}} = \begin{cases} \omega_{\mathrm{d},1} & \text{if} \quad \phi_{\mathrm{g}} \leq \Phi_{\mathrm{g},1} \\ \omega_{\mathrm{d},2} & \text{if} \quad \Phi_{\mathrm{g},1} < \phi_{\mathrm{g}} \leq \sum_i^2 \Phi_{\mathrm{g},i} \\ \omega_{\mathrm{d},3} & \text{if} \quad \sum_i^2 \Phi_{\mathrm{g},i} < \phi_{\mathrm{g}} \leq \sum_i^3 \Phi_{\mathrm{g},i} \end{cases}, \tag{25}$$

where $\omega_{\mathrm{d},1}(t)$, $\omega_{\mathrm{d},2}(t)$ and $\omega_{\mathrm{d},3}$ are the same functions already defined in Section IV-B, ϕ_{g} is the measured generalized flipping angle defined in (15) and $\Phi_{\mathrm{g},1}$, $\Phi_{\mathrm{g},2}$ and $\Phi_{\mathrm{g},3}$ are the same functions already defined in Section IV-B. If the actual generalized flipping angle does not reach $\Phi_{\mathrm{g},1}$ at the end of the first stage of the multi-flip phase of the aerobatic maneuver, then the flipping speed reference is set to $\omega_{\max}$. Similarly, if the generalized flipping angle ϕ_{g} reaches the

[1] Single-Input–Single-Output.
[2] Pulse-Width-Modulation.

TABLE II: Parameters of the Flipping Velocity Reference and Control Gains Used in the Real-Time Experiments.

	$\Phi_{g,1}$ (°)	$\Phi_{g,2}$ (°)	$\Phi_{g,3}$ (°)	ω_{max} (°/s)	k_ω $\times 10^3$	k_α $\times 10^5$
Single Flip ($\boldsymbol{b}_1$)	180	0	180	1400	2	3
Double Flip ($\boldsymbol{b}_1$)	200	300	220	1600	2	3
Triple Flip ($\boldsymbol{b}_1$)	220	520	340	1900	2	3
Single Flip (45°)	180	0	180	1400	2	6
Double Flip (45°)	200	300	220	1600	2	6
Triple Flip (45°)	220	520	340	2500	2	6

target angle before the flipping speed reference becomes zero at the third stage of the process in Fig. 5, then the flipping speed is set to zero immediately.

V. Experimental Results

Experiments are conducted for two cases. The first one is flipping around the body-frame $\boldsymbol{b}_1$ axis and the second one is flipping around a generalized axis that lies on the body-frame $\boldsymbol{b}_1$-$\boldsymbol{b}_2$-plane and deviates from the $\boldsymbol{b}_1$ axis by 45°. All single, double and triple flips are tested under both flipping axes and are set to be $\boldsymbol{a}_f = [1 \quad 0 \quad 0]^T$ and $\boldsymbol{a}_f = [1/\sqrt{2} \quad 1/\sqrt{2} \quad 0]^T$ for the first and second case, respectively. The on-board controller frequency is 500 Hz, and during all the phases described in Section II the robot remains completely autonomous by employing on-board sensors and computational capabilities only. The joystick illustrated in Fig. 4 is manually actuated to compensate for drift on the $\boldsymbol{b}_1$-$\boldsymbol{b}_2$-plane after all three flipping phases are completed. Table II gives the parameters of the planned generalized speed reference and control gains employed during the multi-flip maneuvers about both the principal and non-principal axes. Additionally, k_ω and k_α refer to the diagonal elements in the diagonal control gain matrices K_ω and K_α in (24). Notice that the maximum generalized flipping speed can reach up to $2.5 \cdot 10^3$ deg $\cdot$ s^{-1} about the non-principal axis. This allows the quadrotor to complete a multi-flip maneuver quicker than when flipping about a principal axis.

Figs. 7-(a), 7-(b) and 7-(c) illustrate single-, double- and triple-flip maneuvers around the body-fixed $\boldsymbol{b}_1$ axis by showing the plot of the measured angular velocity of the body-frame $\boldsymbol{b}_1$ axis, the flipping speed reference and the corresponding Euler roll-angle. In this case, the signals Gyro.$\boldsymbol{b}_1$ is the angular velocity about the body-frame $\boldsymbol{b}_1$ axis. Similarly, Figs. 7-(d), 7-(e) and 7-(f) illustrate single-, double- and triple-flip maneuvers around the generalized axis $\boldsymbol{a}_f = [1/\sqrt{2} \quad 1/\sqrt{2} \quad 0]^T$. The signals Gyro.$\boldsymbol{b}_1$ and Gyro.$\boldsymbol{b}_2$ are the angular velocities about the body-frame $\boldsymbol{b}_1$ and $\boldsymbol{b}_2$ axes. Clearly, the angular flipping-speed references about the body-frame $\boldsymbol{b}_1$ and $\boldsymbol{b}_2$ axes are $1/\sqrt{2}$ as large as the generalized flipping speed reference.

The amount of oscillation in the quadrotor's angular velocity at the end of the multi-flip phase of an aerobatic maneuver can be used by the control algorithms to determine if the quadrotor can be re-stabilized successfully before hitting the ground. The angular acceleration feedback control loop significantly reduces the overshoot in the flipping speed signal that appears at the end of an aerobatic maneuver and ensures that the actual flipping speed closely trails the reference speed despite the rotor's rather long settling time, as shown in Fig. 2.

Fig. 8-(a) presents three consecutive successful triple-flip maneuvers around the body $\boldsymbol{b}_1$ axis, demonstrating the robustness of the proposed gain-scheduling-based control method in Fig. 6. Attempting subsequent consecutive triple-flip maneuvers is hindered by the combination of low power density of the quadrotor's battery and high power consumption rate during flip maneuvers. Fig. 8-(b) shows the measured Euler angles associated with a triple-flip aerobatic maneuver.

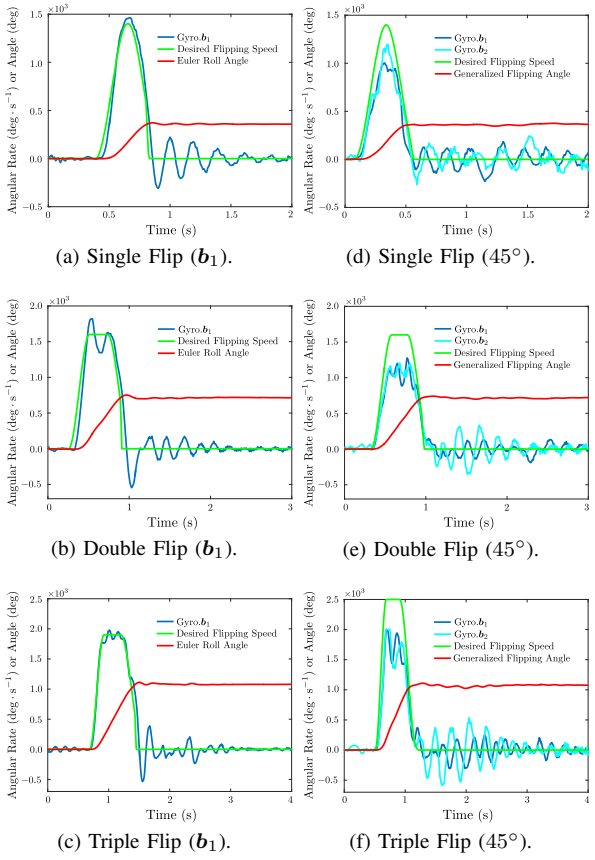

(a) Single Flip ($\boldsymbol{b}_1$). (d) Single Flip (45°).

(b) Double Flip ($\boldsymbol{b}_1$). (e) Double Flip (45°).

(c) Triple Flip ($\boldsymbol{b}_1$). (f) Triple Flip (45°).

Fig. 7: **(a)(b)(c)** Single, double and triple flips about the body-fixed $\boldsymbol{b}_1$ axis. The red line is the measured generalized flipping angle, equal to the Euler roll-angle in this case. The green line is the flipping speed reference and the blue line is the measured angular velocity about the body $\boldsymbol{b}_1$ axis. **(d)(e)(f)** Single, double, and triple flips about the generalized axis that lies in the body-frame $\boldsymbol{b}_1$-$\boldsymbol{b}_2$-plane and deviates 45° from the $\boldsymbol{b}_1$ axis. In this case, since $\boldsymbol{a}_f = [1/\sqrt{2} \; 1/\sqrt{2} \; 0]$, the speed reference for the angular velocities about $\boldsymbol{b}_1$ and $\boldsymbol{b}_2$ is $1/\sqrt{2}$ as large as the generalized flipping speed reference. Gyro.$\boldsymbol{b}_1$ and Gyro.$\boldsymbol{b}_2$ are the measured angular speeds about $\boldsymbol{b}_1$ and $\boldsymbol{b}_2$, respectively.

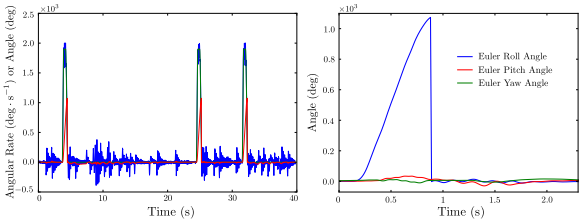

(a) Three Triple Flips. (b) Euler Angles of a Triple Flip.

Fig. 8: **(a)** This plot illustrates a process of three consecutive triple-flip maneuvers about the $\boldsymbol{b}_1$ axis. The Euler roll-angle is shown in red, the flipping speed reference is shown in green and the angular velocity about $\boldsymbol{b}_1$ is shown in blue. The noticeable oscillations of the angular velocity between aerobatic maneuvers are due to the manual compensation of horizontal drift. **(b)** Euler angles measured during the second triple-flip maneuver in Fig. 8-(a). The Euler roll-angle, pitch-angle and yaw-angle are shown in blue, red and green, respectively. During the triple-flip maneuver, the instantaneous pitch-angle maximum drift is 30°. For the other two triple-flip maneuvers, the instantaneous maximum drift angle is less than 10°.

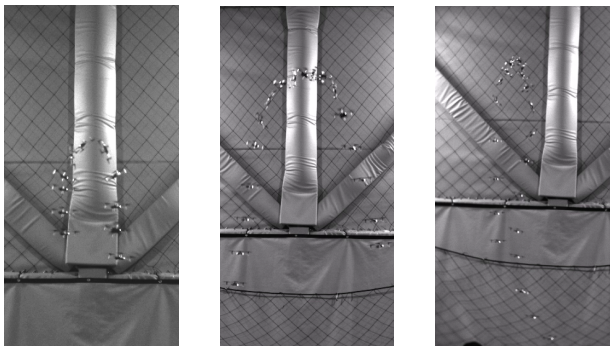

(a) Single flip ($\boldsymbol{b}_1$). (b) Double flip ($\boldsymbol{b}_1$). (c) Triple flip ($\boldsymbol{b}_1$).

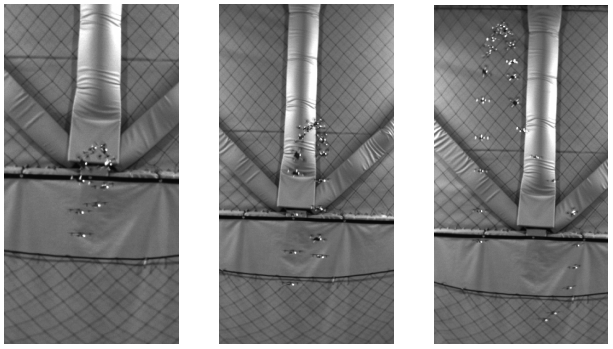

(d) Single flip ($45°$). (e) Double flip ($45°$). (f) Triple flip ($45°$).

Fig. 9: Single-flip, double-flip and triple-flip maneuvers about the body-fixed axis $\boldsymbol{b}_1$ and a $45°$ generalized flipping axis. In these six figures, the multi-flip maneuver stars from the left bottom hand-side and ends at the right bottom hand-side.

Fig. 9 presents the time-lapse plots of six multi-flip experiments. Due to the low thrust-to-weight ratio and aerodynamic disturbances, it can be observed that the descent distance for a triple-flip maneuver is much longer than those associated with single- and double-flip maneuvers. These time-lapse images are selected from videos taken using a high-speed camera at 240 *frames per second* (fps). The complete sequence of experiments can be seen in this paper's accompanying video (also available in [22]).

Since we choose to neglect gyroscopic effects and aerodynamic disturbances when modeling the system, it is not surprising that we have observed attitude deviations from the trajectory references during multi-flip maneuver experiments. For instance, in some occasions when performing a triple-flip experiment, the maximum instantaneous pitch-angle and yaw-angle errors can be as much as $30°$, as can be seen in Fig. 8-(b). Therefore, further study of the gyroscopic effects and aerodynamic disturbances is required to minimize the attitude error. As mentioned earlier, limited power density of the quadrotor's battery together with limited motor's performance can lead to unpredictable reduction in high-speed maneuver control effectiveness.

VI. Conclusions and Future Work

We proposed and experimentally demonstrated the suitability of a simple and robust gain-scheduling-based real-time control strategy for the generation and real-time implementation of high-speed multi-flip aerobatics maneuvers on a fully autonomous 19-gram quadrotor with low thrust-to-weight ratio, operating in the presence of aerodynamic disturbances. To implement the proposed real-time control scheme, we introduced a new speed planning method and the notions of generalized flipping axis and generalized flipping angle. All the experimental results presented here were obtained with the use of algorithms running entirely on-board. The most important experimental result obtained in the course of this research is the successful planning and performance of a control three-flip aerobatic maneuver.

References

[1] R. Mahony, V. Kumar, and P. Corke, "Multirotor Aerial Vehicles: Modeling, Estimation, and Control of Quadrotor," *IEEE Robotics & Automation Magazine*, vol. 19, no. 3, pp. 20–32, 2012.

[2] G. M. Hoffmann, H. Huang, S. L. Waslander, and C. J. Tomlin, "Quadrotor Helicopter Flight Dynamics and Control: Theory and Experiment," in *Proc. AIAA Guidance, Navigation, and Control Conference*, vol. 2, 2007.

[3] Z. T. Dydek, A. M. Annaswamy, and E. Lavretsky, "Adaptive Control of Quadrotor UAVs: A Design Trade Study with Flight Evaluations," *IEEE Transactions on Control Systems Technology*, vol. 21, no. 4, pp. 1400–1406, 2013.

[4] A. Coates, P. Abbeel, and A. Y. Ng, "Learning for Control from Multiple Demonstrations," in *Proc. 25th International Conference on Machine Learning*, 2008, pp. 144–151.

[5] D. Mellinger, N. Michael, and V. Kumar, "Trajectory Generation and Control for Precise Aggressive Maneuvers with Quadrotors," *The International Journal of Robotics Research*, vol. 31, no. 5, pp. 664–674, 2012.

[6] S. Lupashin, A. Schöllig, M. Sherback, and R. D'Andrea, "A simple learning strategy for high-speed quadrocopter multi-flips," in *Proc. IEEE International Conference on Robotics and Automation (ICRA 2010)*, 2010, pp. 1642–1648.

[7] J. H. Gillula, H. Huang, M. P. Vitus, and C. J. Tomlin, "Design of Guaranteed Safe Maneuvers Using Reachable Sets: Autonomous Quadrotor Aerobatics in Theory and Practice," in *Proc. IEEE International Conference on Robotics and Automation (ICRA 2010)*, 2010, pp. 1649–1654.

[8] E. Mueggler, B. Huber, and D. Scaramuzza, "Event-Based, 6-DOF Pose Tracking for High-Speed Maneuvers," in *Proc. IEEE/RSJ International Conference on Intelligent Robots and Systems (IROS 2014)*, 2014, pp. 2761–2768.

[9] S. R. Barros dos Santos, S. N. Givigi Jr., and C. L. Nascimento Jr., "Nonlinear Tracking and Aggressive Maneuver Controllers for Quad-Rotor Robots Using Learning Automata," in *Proc. IEEE International Systems Conference (SysCon 2012)*, 2012, pp. 1–8.

[10] F. A. Goodarzi, D. Lee, and T. Lee, "Geometric Adaptive Tracking Control of a Quadrotor UAV on $SE(3)$ for Agile Maneuvers," *Journal of Dynamic Systems, Measurement, and Control*, vol. 137, no. 9, pp. 091 007–1–12, 2015.

[11] R. M. Murray, D. C. Deno, K. S. J. Pister, and S. S. Sastry, "Control Primitives for Robot Systems," *IEEE Transactions on Systems, Man, and Cybernetics*, vol. 22, no. 1, pp. 183–193, Jan. 1992.

[12] J. S. Shamma and M. Athans, "Analysis of Gain Scheduled Control for Nonlinear Plants," *IEEE Transactions on Automatic Control*, vol. 33, no. 8, pp. 898–907, 1990.

[13] R. Ritz, M. W. Muller, M. Hehn, and R. D'Andrea, "Cooperative Quadrocopter Ball Throwing and Catching," in *Proc. IEEE/RSJ International Conference on Intelligent Robots and Systems (IROS 2012)*, 2012, pp. 4972–4978.

[14] A. P. Schoellig, L. R. Mueller, and R. D'Andrea, "Optimization-Based Iterative Learning for Precise Quadrocopter Trajectory Tracking," *Autonomous Robots*, vol. 33, no. 1, pp. 103–127, 2012.

[15] A. Kushleyev, D. Mellinger, C. Powers, and V. Kumar, "Towards a Swarm of Agile Micro Quadrotors," *Autonomous Robots*, vol. 35, no. 4, pp. 287–300, 2013.

[16] M. Saska, J. Chudoba, L. Precil, J. Thomas, G. Loianno, A. Tresnak, V. Vonasek, and V. Kumar, "Autonomous Deployment of Swarms of Micro-Aerial Vehicles in Cooperative Surveillance," in *Proc. International Conference on Unmanned Aircraft Systems (ICUAS 2014)*, 2014, pp. 584–595.

[17] S.J. Shen, Y. Mulgaonkar, N. Michael, and V. Kumar, "Multi-Sensor Fusion for Robust Autonomous Flight in Indoor and Outdoor Environments with a Rotorcraft MAV," in *Proc. IEEE International Conference on Robotics and Automation (ICRA 2014)*, 2014, pp. 4974–4981.

[18] R. M. Murray, Zexiang Li, and S. S. Sastry, *A Mathematical Introduction to Robotic Manipulation*. CRC Press, 1994.

[19] https://wiki.bitcraze.io/projects:crazyflie:index.

[20] R. Mahony, T. Hamel, and J.-M. Pflimlin, "Nonlinear Complementary Filters on the Special Orthogonal Group," *IEEE Transactions on Automatic Control*, vol. 53, no. 5, pp. 1203–1218, 2008.

[21] J. B. Kuipers, *Quaternions and Rotation Sequences*. Princeton University Press, 1999.

[22] http://www.uscamsl.com/resources/ICRA2016/MultiFlip.mp4.